Article

Evolving Patterns of Hyperfluorescent Fundus Autofluorescence Accompany Retinal Atrophy in the Rat and Mimic Atrophic Age-Related Macular Degeneration

Natalie Pankova[1–3], David Sung Hyeon Baek[1–3], Xu Zhao[2], Hai Wang[2], Matthew-Mina Reyad[2], Huiyuan Liang[2], Rahul Joshi[2], and Shelley Romayne Boyd[1–3]

[1] Department of Ophthalmology and Vision Sciences, University of Toronto, Toronto, ON, Canada
[2] Keenan Research Centre for Biomedical Science, St. Michael's Hospital, Toronto, ON, Canada
[3] Laboratory Medicine and Pathobiology, University of Toronto, Toronto, ON, Canada

Correspondence: Shelley Romayne Boyd, Department of Ophthalmology, St Michael's Hospital, Unity Health, 209 Victoria Street, Toronto, ON, Canada M5H 1T8, Canada.
e-mail: shelley.boyd@unityhealth.to

Purpose: Complex two-dimensional (2D) patterns of hyperfluorescent short-wave fundus autofluorescence (FAF) at the border of geographic atrophy (GA) can predict its expansion in patients with late non-exudative "dry" AMD. However, preclinical models do not phenocopy this important feature of disease. We sought to describe the spatiotemporal changes in hyperfluorescent FAF patterns that occur following acute oxidative stress, potentially in association with GA expansion.

Methods: Sprague Dawley rats ($n = 54$) received systemic sodium iodate (25–45 mg/kg, $n = 90$ eyes) or saline ($n = 18$ eyes) and underwent serial full fundus imaging by confocal scanning laser ophthalmoscopy, including blue FAF and delayed near-infrared analysis. Composite images of the fundus were assembled, and the 2D patterns were described qualitatively and quantitatively. A subset of eyes underwent tissue analysis, and four underwent optical coherence tomography (OCT) imaging.

Results: Reproducibly changing, complex patterns of hyperfluorescent FAF emerge at the borders of toxin-induced damage; however, in the absence of GA expansion, they percolate inward within the region of retinal pigment epithelium loss, evolving, maturing, and senescing in situ over time. Unexpectedly, the late FAF patterns most closely resemble the diffuse tricking form of clinical disease. A five-stage classification system is presented.

Conclusions: Longitudinal, full-fundus imaging of outer retinal atrophy in the rat eye identifies evolving, complex patterns of hyperfluorescent FAF that phenocopy aspects of disease.

Translational Relevance: This work provides a novel tool to assess hyperfluorescent FAF in association with progressive retinal atrophy, a therapeutic target in late AMD.

Introduction

Geographic atrophy (GA) is the late, irreversibly blinding complication of dry age-related macular degeneration (AMD), and there are no approved treatments. Regions of GA appear hypofluorescent (dark) and readily quantifiable using short-wave fundus autofluorescence (FAF) in the blue–green spectrum, supporting use of this measure as both enrollment criteria and an endpoint for late-phase interventional clinical trials.[1–5] In particular, current pivotal phase 3 trials enroll patients with pre-existent GA, and the rate of GA expansion is employed as a measure of efficacy, comparing untreated and treated arms over at least 12 months. Further, to enrich for patients likely to progress during the course of study, enrollment criteria often include the presence of hyperfluorescent (bright) FAF at the border, or in the adjacent junctional zone surrounding the GA.[1,4,6] When present, hyper-

fluorescent FAF indicates disease activity, suggesting both increased likelihood and directionality of GA expansion.[7–12] Although it is widely recognized that endogenous fluorophores such as lipofuscin give rise to the retinal pigment epithelium (RPE) signal,[13,14] the pathogenesis of the differing patterns of hyperfluorescence is not known.

Following from early case studies and later from the prospective Fundus Autofluorescence Imaging in Age-Related Macular Degeneration study of patients with GA, hyperfluorescent FAF patterns can be described as nine distinct phenotypes that differentially predict the rates of future expansion.[7,9,15,16] These complex two-dimensional (2D) FAF patterns are clinically identified by physicians through the process of whole image pattern recognition[17] and, though only recently and rarely quantified, have been analyzed by others and further coalesced into fewer groups, corroborating their association with differential rates of GA expansion.[12,18,19] Accordingly, in the absence of hyperfluorescent FAF, GA is not likely to expand, whereas patterns such as banded (see Fig. 2a), patchy, diffuse non-trickling, and diffuse trickling have the highest rates of GA expansion.[8,9,12,20–22] Despite the importance of hyperfluorescent FAF patterns to patient prognosis and their critical role in clinical trial design, complex FAF patterns are not described in animal models.

Overall, preclinical studies of non-exudative AMD are hampered by a lack of animal models that predict clinical trial success. No species other than *Homo sapiens*, not even non-human primates, develop advanced disease,[23] and genetic models do not adequately capture disease complexity.[24–26] Nonetheless, by studying the tissue process of neovascularization per se, rather than AMD, rodent models have played a critical role in the development of anti-angiogenic treatments for exudative wet AMD.[27–37] Therefore, in the current study we elected to study the tissue process of retinal atrophy rather than AMD, and we sought to determine, using repeated in vivo confocal scanning laser ophthalmoscopy (cSLO) imaging, whether hyperfluorescent patterns occur at the distal borders of GA and beyond and if they predict or accompany GA expansion.

Sodium iodate ($NaIO_3$) is a strong oxidizing agent that, even when administered systemically, has marked relative specificity for the eye, causing acute RPE necroptosis followed by a period of photoreceptor apoptosis and outer retinal thinning.[38,39] It has been employed by vision scientists for many decades and is a widely used model of atrophy.[40–43] Unfortunately, the ocular toxicity of $NaIO_3$ is also known to be directly relevant to the human biology, having been inadvertently administered to patients undergoing treatment for pneumothorax, with ensuing bilateral, macula-specific vision loss.[44]

More recently, cSLO imaging has been applied to the $NaIO_3$ model to enhance decades of histological study. To date, FAF imaging has led to descriptions of hyperfluorescent dots, spots, punctate lesions and non-uniformity of signal, that bear some, but limited semblance to disease.[42,43,45] Further, application of optical coherence tomography (OCT) to the $NaIO_3$ model has confirmed the histologically reported sequence of early RPE loss, followed by progressive outer retinal thinning and the accumulation of subretinal debris.[42,46,47] However, highlighting the difference between the evolution of the $NaIO_3$-induced atrophy and the development of clinical GA, the application of high-resolution OCT to patients with nascent GA has shown that RPE loss does not occur first as it does in the $NaIO_3$ model but rather last, preceded by early subsidence and progressive thinning of the outer retina.[48] Based on these highly reproducible OCT findings, the Classification of Macular Atrophy (CAM) Consensus working group redefined GA[49] and developed a classification system that describes sequential loss of outer retina and RPE into four stages, proceeding from incomplete outer retinal atrophy (iORA), to complete ORA (cORA), then incomplete RPE + cORA (iRORA), and finally complete RORA (cRORA) when the RPE is finally lost.[48,49] An appealing aspect of this observation is that with RPE remaining as the last layer of full-thickness photoreceptor and RPE loss (PhR/RPE) loss, it could be responsible for the hyperfluorescent signal at the border and in the junctional zones of expanding GA and for residual signal within areas of incomplete GA.

To address the lack of preclinical models of complex hyperfluorescent FAF, this study describes the spatiotemporal changes in blue FAF that accompany RPE loss and outer retinal atrophy following systemic $NaIO_3$ in the Sprague Dawley (SD) rat. By reverse translation from clinical observation to the lab, we hypothesized that regions of PhR/RPE loss will appear dark but their peripheral borders and adjacent junctional zones will appear bright and exhibit complex 2D patterns that may in turn predict or accompany GA expansion. We also used delayed near-infrared analysis (DNIRA) to enhance visualization of the rodent RPE layer (and areas of its loss) in vivo[50] and immunohistochemistry (IHC) to confirm RPE loss. We also applied OCT in a subset of animals to correlate the en face fluorescence with cross-sectional findings. Finally, by engaging four retina specialists familiar with late dry AMD, we compared the patterns of hyperfluorescent FAF observed in the rat against standardized images that qualitatively describe clinical disease to determine the most similar features and phenotypes.

Methods

Animals

Fifty-four adult, albino SD rats, 6 to 7 weeks of age, were obtained from Charles River Laboratories (Wilmington, MA) and exposed to a 12-hour light/dark cycle. To avoid excessive exposure to overhead lighting, animals were housed on the lowest shelves. All experiments were performed in accordance with guidelines set forth by the ARVO Animal Statement for the Use of Animals in Ophthalmic and Vision Research, and animal protocols were approved by the local animal care committee.

Sodium Iodate

Sodium iodate (Sigma-Aldrich, St. Louis, MO) was prepared fresh daily at a stock solution of 45 mg/mL in injectable saline (Baxter Canada; Mississauga, ON, Canada). On day 0 of experimentation, the stock $NaIO_3$ solution was diluted to final concentrations of 25 to 33 mg/mL or 45 mg/mL, and animals received dosages of 25 to 33 mg/kg or 45 mg/kg, administered intravenously (IV) via tail vein. These two dosages, designated low or high, were selected to induce small-size or large regions of GA-like atrophy, respectively. Control (i.e., non-$NaIO_3$ challenged) animals received normal saline via tail vein or nothing.

In Vivo Imaging

Animals were anesthetized with a combination of ketamine (100 mg/kg) and xylazine (10 mg/kg), and pupils were dilated with a single drop of 0.8% tropicamide in 5% phenylephrine hydrochloride solution (Diophenyl-T; Sandoz Canada, Boucherville, QB, Canada). GenTeal lubricating eye drops (Novartis, Basel, Switzerland) were repeatedly applied to the corneal surface during all procedures.

Fundus imaging was performed using a Heidelberg Retina Angiography 2 (HRA2) system (Heidelberg Engineering, Heidelberg, Germany). Lacking OCT functionality, this device has brighter luminance in the infrared (IR) spectrum than instruments with light deflected for this purpose. During imaging, a 30° lens was used, and photographs were first acquired using IR reflectance (820 nm) to determine the general plane of focus and adjusted thereafter for FAF and DNIRA. Eyes were screened prior to initiating experiments to exclude those with significant pre-existent lesions and to confirm normal baseline retinal structure. Limited OCT analysis was performed (*n* = 4 animals) using a rodent-specific device (see below).

To visualize potential GA-like atrophy expansion and distal hyperfluorescent borders, we performed extensive realignment of the animal, pupillary axis, and imaging beam to acquire multiple images throughout the entire fundus, including the far periphery. These images were obtained in addition to the traditional emphasis on the region adjacent to the optic nerve head (ONH).[45,51,52] When assembled, the resultant composite images enable study of the total area of GA-like atrophy, the distal and proximal border of GA-like atrophy, and, where possible, the regions beyond.

Fluorescein and Indocyanine Green Angiography

Because fluorescein dye can interfere with FAF imaging, fluorescein angiography was not used except to demonstrate differences between DNIRA and other forms of routine imaging (see Fig. 2). When applied (*n* = 2 animals), it was performed using 2000-kD fluorescein dextran, injected IV via the tail vein. By contrast, indocyanine green (ICG) angiography (0.35 mg/mL in sterile saline, injected to a final dose of 0.35 mg/kg) was performed in all animals at the initial fundus screening, at 2 or occasionally 3 days prior to $NaIO_3$ injection, to evaluate the vasculature and as part of the DNIRA protocol.

Delayed Near-Infrared Analysis

As originally described,[50] DNIRA was performed by the systemic delivery of ICG dye (0.35 to 2.0 mg/kg) in the days and weeks prior to in vivo imaging in the corresponding near-infrared (NIR) excitation and emission spectra (790 nm and 810 nm, respectively), the ICG channel (Fig. 1), without further injection of dye. We demonstrated that this delay between dye injection and imaging permits detection of ICG dye that has accumulated within the rat RPE layer following systemic administration and, critically, diminution of the background signal. The net effect is significant enhancement of the signal-to-noise ratio of the DNIRA in detection of RPE, over the relatively low levels observed using FAF. Accordingly, to define the full extent of RPE loss, $NaIO_3$ was injected 2 to 3 days after ICG angiography, 0.35 mg/kg via the tail vein, and DNIRA imaging was performed at days 3, 7, and 14 after $NaIO_3$ in the ICG channel, without further dye injection. When DNIRA was applied to later timepoints (day 28 or later after $NaIO_3$), ICG dye was again delivered systemically, 2 to 3 days prior to imaging in the ICG channel, without further injection of dye (for the time course of imaging, see Fig. 1f).
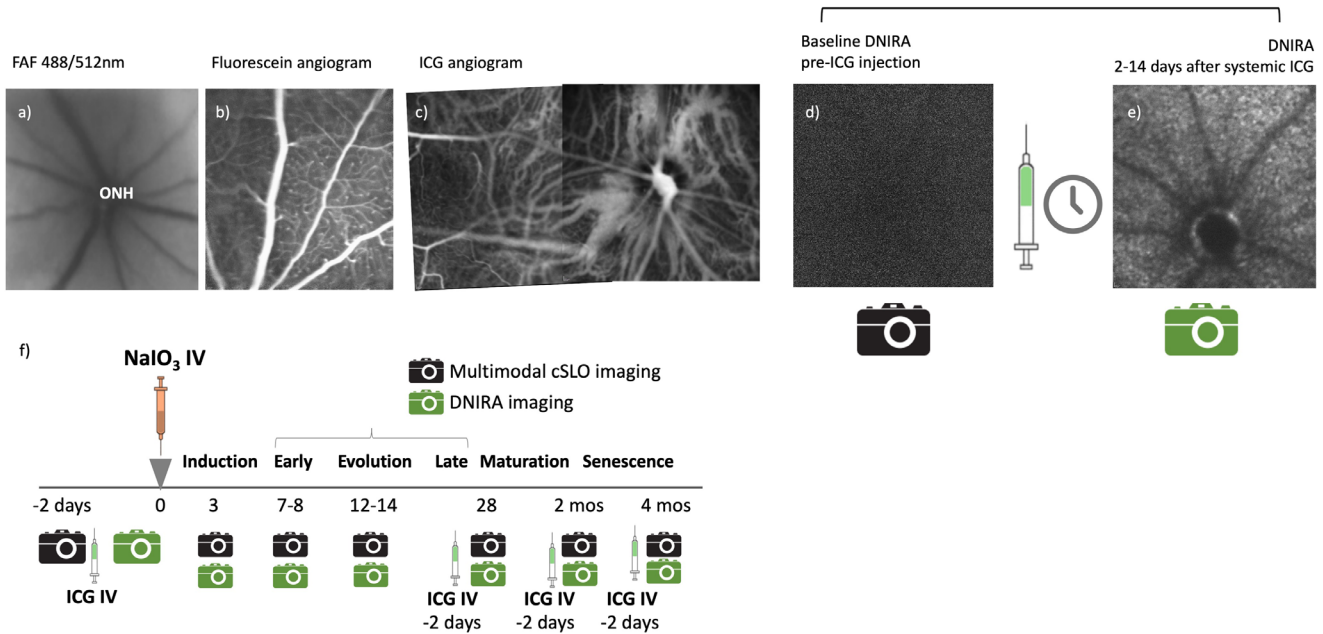
Figure 1. cSLO imaging confirmed multimodal findings in the normal SD rat eye and demonstrated that DNIRA is distinct from routinely used modalities. (a) In the SD rat eye, blue short-wave FAF (excitation, 488 nm; emission, 500 nm) showed a diffuse ground-glass glow that was absent at the ONH and in radial lines corresponding to overlying blood vessels, supporting its use as the gold standard for detection of the RPE. (b) Fluorescein angiography demonstrated the radial inner retinal blood vessels. (c) ICG angiography (excitation, 790 nm; emission, 810 nm) clearly demonstrated the choroidal vasculature. These methods are distinct from DNIRA (d, e), which was also visualized in the ICG excitation and emission spectra. (d) When using DNIRA, there was no or negligible signal prior to dye injection (images were taken using the highest cSLO energy level, "gain," to activate image acquisition). (e) Images acquired 2 or 3 (or up to 14) days after systemic ICG injection, without further injection of dye, showed a finely speckled, diffuse fluorescence that, like FAF, was absent at the ONH and in the location of overlying retinal blood vessels. Fluorescein angiography was performed for illustrative purposes only ($n = 2$ eyes), and never preceded FAF. (f) Time course of DNIRA and multimodal cSLO imaging used in this study. In addition to FAF, indicated by the *black camera icon*, and ICG angiography, indicated by the *green syringe*, the DNIRA images were acquired out to 14 days after the initial (pre-NaIO₃) ICG injection (*green camera icon*). For later timepoints, performed at 1, 2, and 4 months, ICG dye was again administered systemically 2, or occasionally 3, days prior to subsequent multimodal image acquisition, without further injection of dye.

Optical Coherence Tomography

Though our HRA2 was not equipped with OCT capabilities, we benefited from the temporary loan of a rodent-specific device (Bioptigen Envisu R2200; Leica Microsystems, Wetzlar, Germany). Images were acquired with a density of 1000 a-scans $\times$ 1000 b-scans, using a radial arm of approximately 1000 μm. Applied to multiple regions of interest in four eyes, multiple high-resolution images were acquired and analyzed both in cross-section (z-axis) and in en face slabs (volume intensity projections) through the retina.

Post Hoc Image Analysis and Analysis of Atrophy

Following export, the HRA2 images were manually assembled into composites with an attempt to best juxtapose images with near-equivalent levels of illumination, using the vasculature as markers. Due to the curvature of the eye and small pupillary aperture, this was often not possible across all edges of the image. Nonetheless, composite images were described both qualitatively and quantitatively. Quantification of regions of atrophy was performed two ways. First, we compared the size (area) of the NaIO₃-induced patches at the first and final imaging sessions, looking for potential expansion, noting that portions of the peripheral borders of large patches often extended beyond image capture, underestimating their full size. Second, we performed threshold analysis of the area of hyperfluorescent signal within the entire image (described below), which was compared against the total area of the image. Qualitative description of the complex 2D patterns was performed through the development of a staging system (as described in Results).

Quantitative Analysis of the Hyperfluorescent Signal

Individually acquired FAF cSLO images were analyzed using ImageJ 1.48 (National Institutes of Health, Bethesda, MD) and Java 1.6.0_24 (64-bit), using an 8-bit image format. Background subtraction (rolling ball radius 50–150 pixels) was performed to eliminate noise. An image threshold was adjusted (minimum, 0; maximum, 243) to set a basal level of autofluorescence, and measurements expressed as percentage of hyperfluorescent area over total area, both measured in pixels. The percent area of hyperfluorescent signal per image was then compared between stages of change after $NaIO_3$ (described below).

Fluorescent Immunohistochemistry

To histologically confirm regions of RPE loss in areas of $NaIO_3$-induced PhR/RPE damage, animals were euthanized, and wholemount posterior eyecups were evaluated by fluorescent IHC. Following enucleation and removal of the anterior segment, posterior segments devoid of the lens were fixed in 4% paraformaldehyde in phosphate buffered saline (PBS) for 45 to 60 minutes, and, after being rinsed again with PBS, they were transferred to cold methanol and stored at –20°C until use. Following removal of the retina, the presence or absence of the RPE was identified in wholemount posterior eye cups by blocking with 5% bovine serum albumin in PBS with 0.1% Triton X-100 (Sigma-Aldrich) for 1 hour at room temperature. Eye cups were then incubated with primary antibodies against RPE65, diluted 1:200 in blocking buffer (mouse monoclonal anti-RPE65 antibody, ab78036; Abcam, Cambridge, UK) and incubated at 4°C overnight on a shaker. After they were washed four times for 20 minutes each in 1× PBS, the samples were again subjected to blocking buffer for 1 hour at room temperature. Eye cups were next incubated with a 1:400 dilution of Invitrogen Goat anti-Mouse IgG (H+L) Highly Cross-Adsorbed Secondary Antibody, Alexa Fluor 555 (A-21424; Thermo Fisher Scientific, Waltham, MA) secondary antibody solution overnight at 4°C with gentle rotation. After they were washed in 1× PBS four times for 20 minutes each, the samples were counterstained with nuclear dye, 4′,6-diamidino-2-phenylindole (DAPI), and mounted in anti-fade fluorescence mounting medium (ab104135; Abcam) on polytetrafluoroethylene-printed two-well sides (Electron Microscopy Sciences, Hatfield, PA). RPE cells were identified by their expression of RPE65 and their unique binucleate appearance. Images were captured using a Zeiss LSM700 confocal microscope (Carl Zeiss Meditec, Jena, Germany) with ZEN Black 2012 software.

Quantitative Polymerase Chain Reaction and Polymerase Chain Reaction Array Analysis

To confirm the in vivo observation that low- and high-dose $NaIO_3$ differentially induces small and large regions of RPE loss, respectively, total RNA was isolated from posterior eyecups ($n = 3$ per group) at 2 weeks, and RPE65 gene expression levels were compared against baseline. After enucleation, eyes were dissected in cold RNAlater solution (Life Technologies, Carlsbad, CA), and the retina, RPE, and choroid were stored in the RNAlater solution. Total RNA was isolated using Invitrogen TRIzol Reagent following the manufacturer's protocol (Thermo Fisher Scientific). If required, total RNA was further purified with the RNeasy MinElute Cleanup kit (Qiagen, Hilden, Germany). The quantity and quality of the RNA were confirmed using a NanoDrop 2000 spectrophotometer (Thermo Fisher Scientific) and Agilent 2100 Bioanalyzer (Agilent Technologies, Santa Clara, CA).

cDNA was synthesized using the Qiagen RT^2 First Strand Kit with 2 μg of total RNA per reaction. Real-time polymerase chain reaction (PCR) was performed using the Qiagen 384-Well Custom RT2 Profiler PCR Array and Qiagen RT^2 SYBR Green ROX qPCR Mastermix with 10 ng cDNA per well. The reactions were run on an Applied Biosystems ViiA 7 Real-Time PCR System (Thermo Fisher Scientific) with default cycling conditions. Differences in gene expression were analyzed using the Qiagen RT^2 Profiler PCR Array Data Analysis v3.5 web portal (http://pcrdataanalysis.sabiosciences.com/pcr/arrayanalysis.php) based on the $\triangle\triangle CT$ method and normalized to peptidyl-prolyl *cis–trans* isomerase H (PPIH) as a reference gene. Primer sequences are proprietary (Qiagen), with details as follows: RPE65 (NM_053562), amplicon start site at position 659 and amplicon size 125 base pairs (bp) (Qiagen catalog no. PPR52080B); and PPIH (XM_001073803), amplicon start site at position 127 and amplicon size of 54 bp (Qiagen catalog no. PPR57387B).

Comparison Between Complex Patterns of FAF in Clinical Disease Versus SD Rat

As AMD is a chronic disorder, composite fundus images from rats that received $NaIO_3$ challenge at least 28 days earlier were presented to four retina specialists,

three of whom were not involved in the study. Each composite rat image was accompanied by one clinical reference image pattern,[7,9,19,53] and after 18 unique presentations, clinicians were asked to identify those with the highest degree of similarity based on their clinical acumen.

Statistical Analysis

Unless otherwise indicated, statistical analysis was performed using Prism 5.0 (GraphPad, San Diego, CA). The relationship between the size of the patch of $NaIO_3$-induced atrophy between imaging sessions was analyzed using a two-tailed, paired Student's *t*-test, and results are presented both as paired data (estimation plot) and the mean of differences. Statistical analysis of the influence of $NaIO_3$ dose (high, low, or none) on the resulting patch size, either large (>1/2 fundus) or small, was performed using Somers' D test for categorical data, and SPSS Statistics 27.0.1.0 (IBM, Armonk, NY). Analysis of quantitative PCR data was based on the replicate $2^{-\triangle\triangle CT}$ values for the gene of interest compared with control (non-$NaIO_3$), and findings were normalized against cyclophilin H (PPIH) using the Relative Expression Software Tool, Multiple Condition Solver (REST-MCS, version 2), with statistical analysis performed based on the protocol by Pfaffl et al.[54] For quantitative image analysis, differences in the percent of image area exceeding threshold brightness were compared between timepoints and between superior and inferior fundus, using an unpaired two-tailed Student's *t*-test. Statistical significance was preset at $P < 0.05$ for all analyses.

Results

First, during prescreening of control, non-$NaIO_3$-challenged eyes ($n = 18$) and $NaIO_3$-challenged eyes ($n = 90$), cSLO imaging confirmed the normal, baseline fundus features of SD rats as previously described (Fig. 1).[55] In particular, blue light FAF showed a diffuse, ground-glass appearance with absence of signal at the ONH and in the location of overlying retinal blood vessels (Fig. 1a), consistent with the presence of autofluorescent bisretinoids such as lipofuscin within the RPE monolayer and with findings in the human eye.[13,15,56–62] Accordingly, FAF is the gold standard for detection of the RPE. Fluorescein angiography, performed in just two animals for illustrative purposes, showed the normal retinal vasculature (Fig. 1b), whereas ICG angiography, performed in all animals 2 or 3 days prior to $NaIO_3$, signifi-

cantly enhanced visualization of the choroidal vessels (Fig. 1c). Also, immediately prior to ICG angiography, baseline DNIRA images, acquired in the NIR excitation and emission spectra (790nm and 810 nm, respectively) before injection of dye, had little or no detectable signal (Fig. 1d), in some cases precluding image capture. However, as previously described, cSLO imaging in the ICG channel performed 2 to 14 days after ICG delivery, but with no further injection of dye, showed that the RPE monolayer was highly visible as a relatively homogeneous fluorescent signal (Fig. 1e).[50] Like FAF, the normal DNIRA signal was absent at the ONH and blocked by overlying retinal blood vessels. Application of DNIRA therefore enhances visualization of the RPE layer, as confirmed in the clinical setting in conjunction with adaptive optics.[50,63,64] As such, and as employed in the following experiments, it is distinct from other routinely used imaging modalities and makes regions of RPE loss highly visible. The time course of in vivo cSLO imaging, relative to $NaIO_3$ and ICG injection, is provided in Figure 1f.

Next, we applied cSLO imaging to rat eyes challenged with $NaIO_3$, with the ultimate goal of comparing the spatiotemporal changes in FAF patterns against those observed in patients with pre-existent GA. For comparison, a representative clinical image of a patient with GA and the banded pattern of hyperfluorescent FAF are shown in Figure 2a.

Reasoning that small patches of $NaIO_3$-induced damage would be easier to photograph to their distal borders than large patches, we delivered low-dose $NaIO_3$ (25–33 mg/kg) by IV injection. Analysis of FAF composite images assembled from throughout the fundus indicated that areas of $NaIO_3$-induced atrophy were indeed small (less than half the fundus) and did not appear hypofluorescent in the rat eye, as in patients with GA. Instead, as shown in a representative composite FAF image taken 3 days after administration of the low-dose $NaIO_3$, a small region of nearly normal fluorescence adjacent and inferior to the ONH was identified by its slightly enhanced border (Fig. 2b). By 7 days after administration of the $NaIO_3$, FAF imaging of this same representative eye demonstrated the emergence of complex, alternating iso- and hyperfluorescent curvilinear patterns (Fig. 2c) along its borders, in the absence of marked hypofluorescence. Given that $NaIO_3$ is well known to induce full thickness loss of both RPE and outer retina,[40,46,47,65–71] this result of increased, rather than decreased, FAF was unexpected compared with clinical findings. It does, however, support preliminary findings by our group.[72]

To confirm that the RPE was indeed lost within this region of hyperfluorescent signal, we performed both DNIRA and terminal IHC, focusing on early
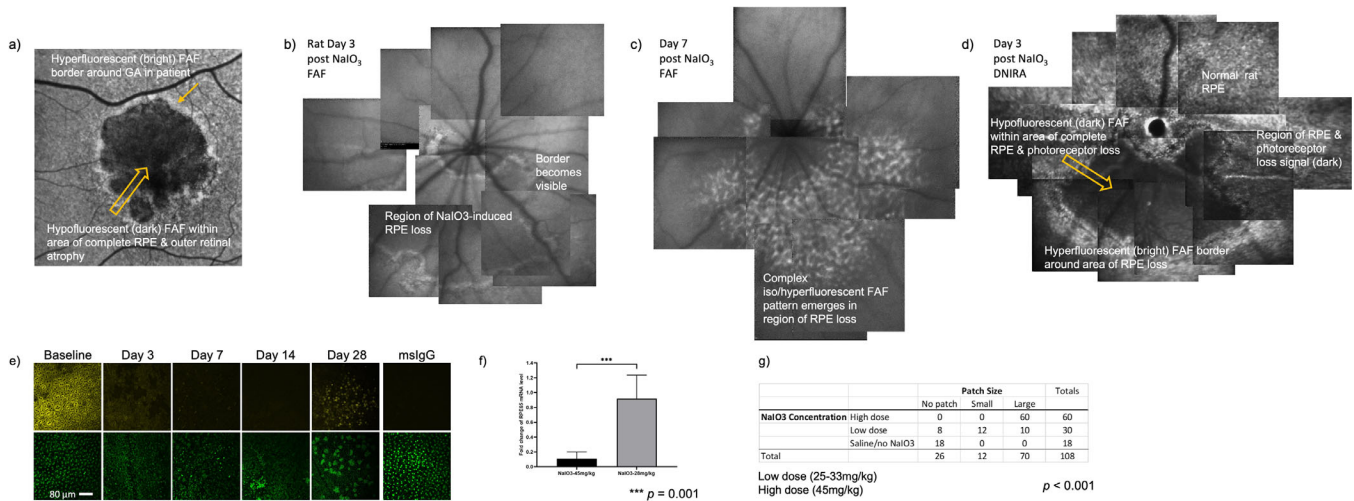
Figure 2. Representative composite blue FAF images taken after low-dose NaIO$_3$ (28 mg/kg, IV) show a small region of RPE damage that was hyperfluorescent rather than hypofluorescent, as expected in the clinical setting. This region was found to be profoundly hypofluorescent with the use of DNIRA. (a) Blue FAF image of a patient with a central region of GA shows a distinct area of hypofluorescence (dark) surrounded by a hyperfluorescent (bright) border. (b) In the rat eye, a representative composite blue FAF image obtained 3 days after low-dose NaIO$_3$ (28 mg/kg, IV) shows a small well-circumscribed region of isofluorescence with a subtle, hyperfluorescent border. This region is inferior and adjacent to the ONH. (c) By 7 days after the administration of NaIO$_3$, a curvilinear pattern of alternating hyper- and isofluorescent FAF emerged. (d) By contrast, using DNIRA in the same eye (representative image from day 3), the area of damage was profoundly hypofluorescent relative to the surrounding signal, was distinct from the FAF image, and more closely resembled the hypofluorescent FAF of clinical GA. (e) Fluorescent IHC images of excised posterior eyecups confirmed the presence of a normal, diploid RPE monolayer in control (non-NaIO$_3$-challenged) eyes ($n = 18$) using nuclear staining (DAPI) and anti-RPE65 antibodies. (e) By contrast, fluorescent IHC images taken in the region of damage at days 3, 7, 14, and 28 after the administration of NaIO$_3$ show that the RPE was rapidly lost, with some indication of potential RPE regeneration by day 28; same-species immunoglobulin G (IgG) control produced no signal. Original magnifications, 20$\times$ and 40$\times$ (note that the lower magnification images have been enlarged for consistency). (f) Similarly, and confirming RPE loss, RPE65 messenger RNA (mRNA) was dose-dependently reduced by NaIO$_3$ challenge, here shown after 14 days (fold change $\pm$ SEM, $P < 0.001$). (g) However, using composite FAF imaging, the two doses of NaIO$_3$ differentially induced large areas of damage ($>1/2$ fundus) in 100% of eyes at 45 mg/kg ($n = 60$), and variably induced large, small, or no areas of damage at the lower doses of 25 to 33 mg/kg ($n = 30$), in approximately a third of eyes each (Somers' D test, $P < 0.001$ for categorical data), indicating that the area of atrophy correlated with NaIO$_3$ dose.

timepoints prior to any potential RPE regeneration that could occur in the rodent eye. Accordingly, and in contrast to FAF, DNIRA imaging of the same eye taken at day 3 showed a well-defined region of hypofluorescent signal (Fig. 2d) with sharp borders more closely resembling clinical GA than did FAF. Consistent with early reports of DNIRA, this observation supports regional loss of the RPE monolayer.[50] Further, fluorescent IHC performed following terminal experimentation and enucleation confirmed that the NaIO$_3$-challenged eyes were devoid of RPE within the region of bright FAF and dark DNIRA, with loss of their duplet nuclear signal and RPE65 immunolabeling (Fig. 2e). NaIO$_3$-induced RPE loss is also supported by significant RPE65 mRNA loss, more so with high-dose NaIO$_3$ challenge than low, compared at 2 weeks (Fig. 2f). In all cases in which a small patch of tissue loss was induced, it was always adjacent to but not contiguous with, and inferior to, the ONH.

Despite the advantage of using low-dose NaIO$_3$ to evaluate the distal borders of small areas of atrophy, we found that they are difficult to reliably induce, occurring in fewer than one-third of eyes (small patch/low dose, $n = 12/30$ eyes, 25–33 mg/kg NaIO$_3$), due to a tendency to either encompass the entire fundus (large patch/low dose, $n = 10/30$ eyes) or not form at all (no patch/low dose, $n = 8/30$ eyes) (Fig. 2g). By contrast, high-dose NaIO$_3$ (45 mg/kg) induced large regions of damage in 100% of the eyes (large patch/high dose, $n = 60/60$; overall $P < 0.001$). Accordingly, with the use of high-dose NaIO$_3$, we reliably observed large regions of damage that encircled the ONH a full 360° and extended to the far retinal periphery (Figs. 3a–3c), but in some cases precluding detection of their entire distal border. Nonetheless, like the smaller lesions, these large areas of RPE loss did not appear dark compared with the background fluorescence using FAF as hypothesized, but rather, as shown in representative serial composite images taken at days 3, 7, and 14 after the administration of NaIO$_3$, displayed the same evolving changes of iso- and hyperfluorescent FAF. In particular, faintly hyperfluorescent
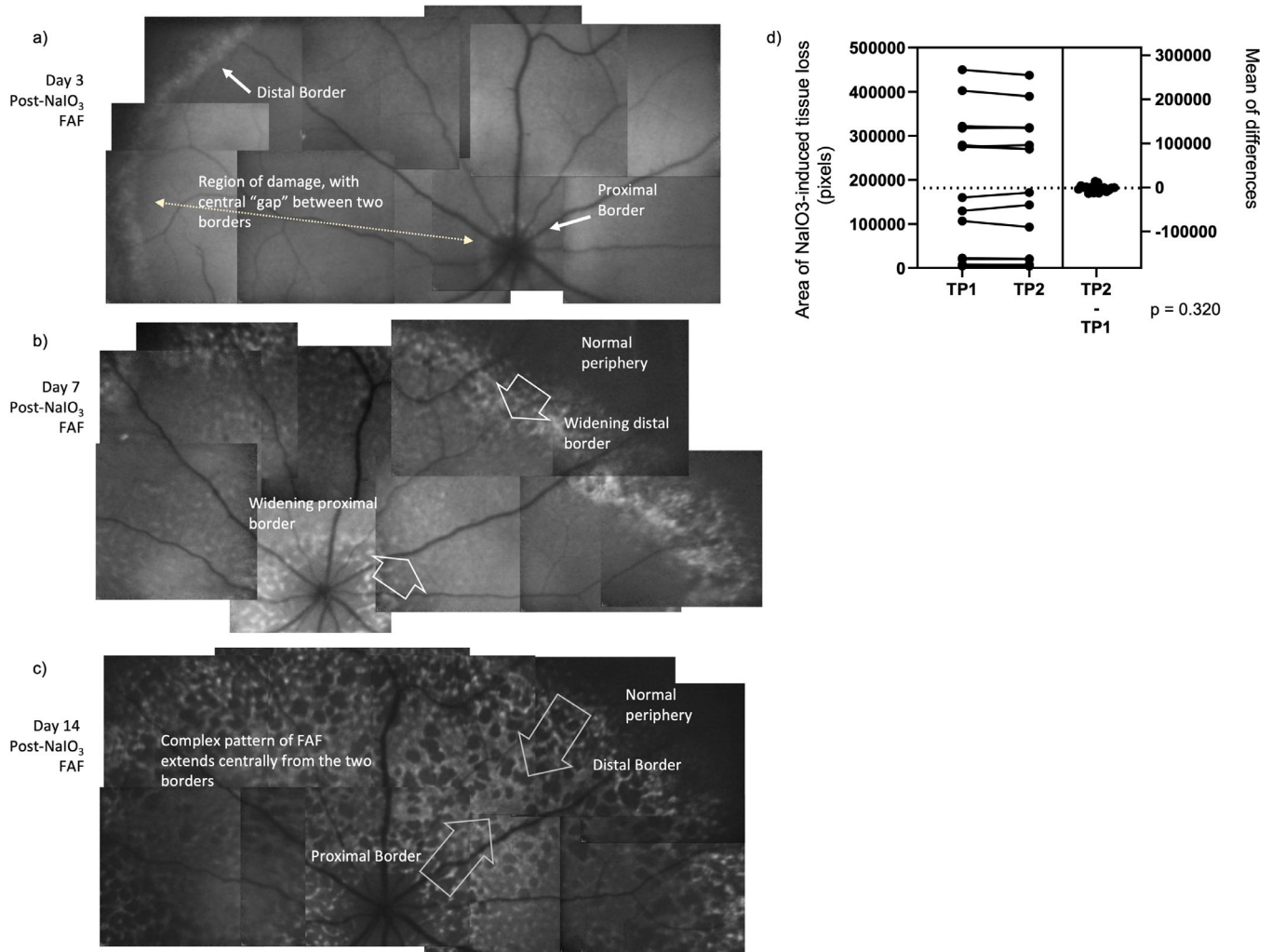
Figure 3. Representative composite blue FAF images taken of the same eye at days 3, 7, and 14 after the administration of high-dose $NaIO_3$ (45 mg/kg, IV) show the emergence and evolution of increasingly complex 2D patterns of hyper- and isofluorescence within a large area of the fundus (superior fundus only shown). (a) Three days after the administration of $NaIO_3$, two narrow slightly hyperfluorescent FAF arcs (or rings, in full 360° view) can be seen immediately surrounding the ONH and the proximal border, and in far retinal periphery at the distal border (*small white arrows*). (b) By 1 week, these hyperfluorescent borders widened and assumed a complex curvilinear pattern of alternating hyper- and isofluorescent signal. (c) By 2 weeks after the administration of $NaIO_3$, these complex patterns extended inward into the region of damage from both borders (*open arrows* show the direction in which the evolving patterns of FAF migrated into the mid-region of damage). (d) In all cases where the border can be viewed, no gross atrophy expansion was observed (84/84 eyes), and no expansion could be measured using paired composite images, where the area of tissue loss (expressed in pixels) measured at timepoint 1 (TP1) was separated by up to 25 days from timepoint 2 (TP2) ($P = 0.320$ for all patches, $P = 0.2634$ for small patches, and $P = 0.3653$ for large patches; evaluated using paired estimation analysis and mean of difference).

borders became evident (Fig. 3a) at days 3 and 4 after the administration of $NaIO_3$, both in the peripapillary region and at the peripheral extent of damage. Over the next 7 to 14 days, these proximal and distal borders widened and developed complex hyperfluorescent FAF patterns, leaving a central area not yet obviously involved. (Figs. 3b, 3c). In the weeks thereafter, the complex hyperfluorescent patterns progressively percolated inward into the region of PhR/RPE loss (days 14–28). In another representative example using high-dose $NaIO_3$ (45 mg/kg), this time comparing early (1 week) and later (1 month) timepoints in the same animal, the complex hyperfluorescent FAF patterns again emerged at the proximal and distal borders (Fig. 4a) and gradually expanded inward to completely fill the gap or mid-region of RPE loss (Fig. 4b) where they further matured in situ. Of note, in none of the $NaIO_3$-challenged eyes that developed patches of atrophy did they expand grossly over time ($n = 82/82$) (Figs. 2–5), an observation supported by
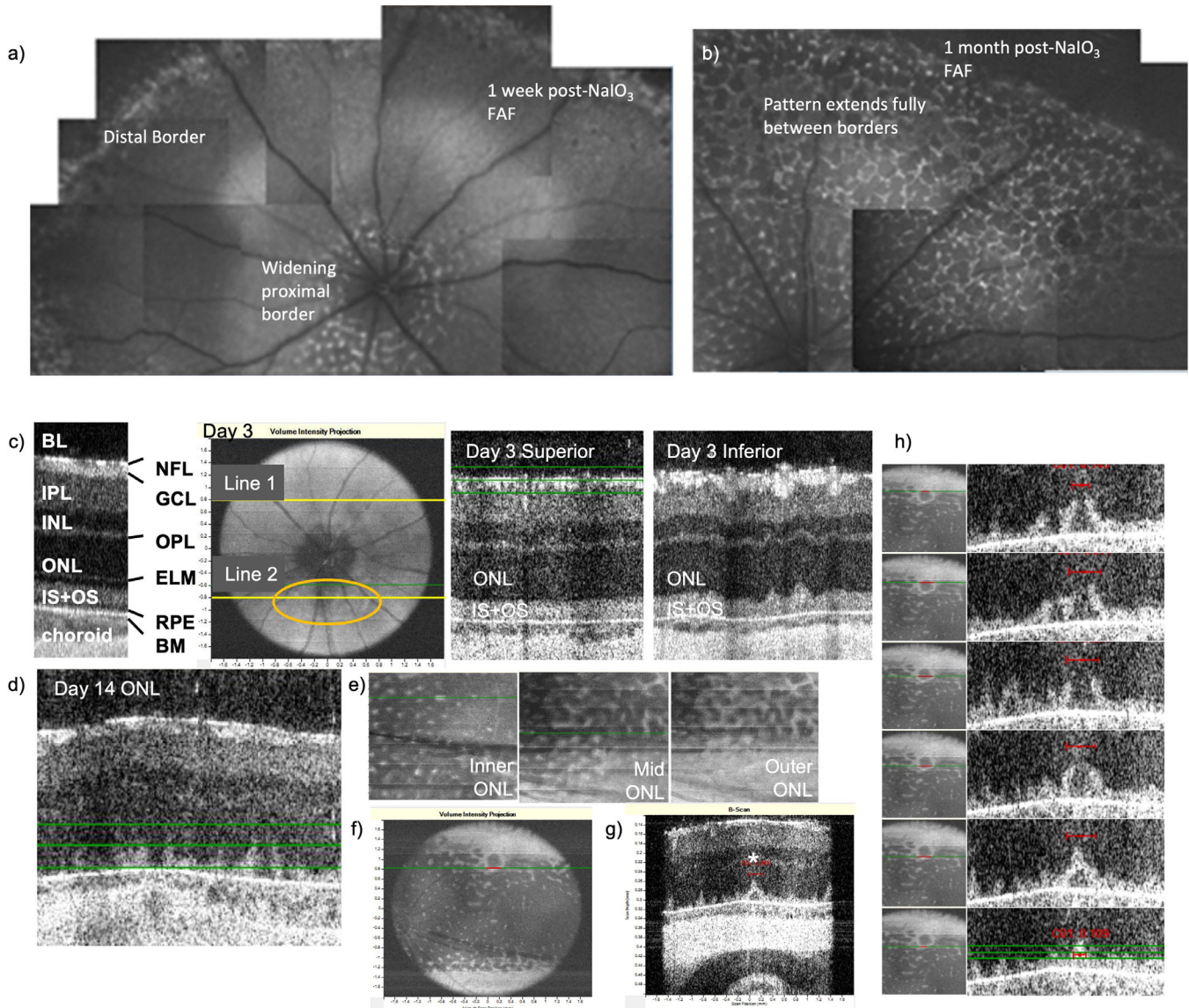
Figure 4. Representative composite images taken at 1 week and 1 month (28 days) after the administration of NaIO$_3$ in the same eye demonstrate the in situ evolution and maturation of complex 2D FAF patterns, whereas representative OCT slab analysis show concordance with the subretinal signal. (a) As previously shown in its early evolution (day 7), the narrow proximal and distal borders widened, and hyperfluorescent FAF patterns emerged and percolated inward to the central region of damage. (b) By 1 month, complex 2D patterns were mature and filled the entire region between the two borders. (c) High-resolution OCT comparing normal (day 0) and early (day 3) rat fundus confirmed loss of the faint, dark RPE band after NaIO$_3$ administration, which in this case is evident in the inferior peripapillary region and not the superior peripapillary region. (d) By day 14 after NaIO$_3$, OCT images acquired near the distal border of the region of damage revealed the appearance of hyperreflective base-down triangles and spikes, which are also evident in (e), by using OCT slab analysis through the reconstructed block taken at slightly different depths in the outer retina. (f, g) Images show the correspondence between en face and cross-sectional OCT signal corresponding to an obvious, distinct ovoid/circular structure and illustrating a hollow-centered, base-down triangle (asterisk; also see asterisk in Fig. 5d). A smaller second circle can be seen with close observation. (h) Multiple b-scans through this region, shown both in the *z*-axis and in the en face projection.

careful measurements of composite images across 17 paired imaging sessions ($n = 34$ composite images, $P = 0.320$) (Fig. 3d).

Next, to preliminarily address the in vivo cross-sectional changes in retinal morphology that correspond to the changing patterns of FAF, we used a rodent-specific, high-resolution OCT device (Bioptigen). Four eyes were evaluated at multiple regions of interest, using multiple b-scans.

Consistent with published reports of NaIO$_3$ toxicity, high-resolution OCT showed loss of the RPE band as early as 3 days after NaIO$_3$.[45,69,73] In the represen-
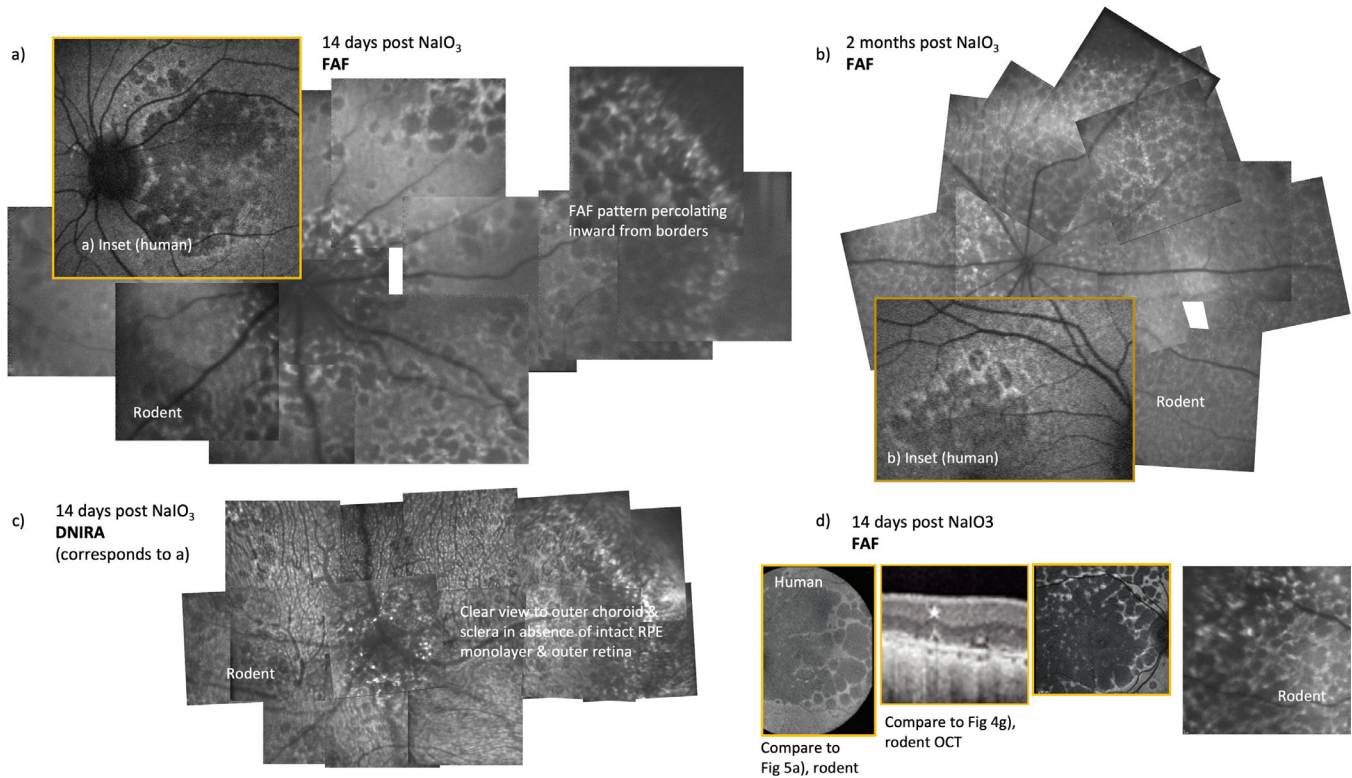
Figure 5. Representative composite images acquired after systemic NaIO$_3$ demonstrate curvilinear patterns of hyperfluorescent FAF that bear similarity to human disease. (a) Representative composite FAF image obtained 14 days after NaIO$_3$ shows complex curvilinear, ovoid patterns evolving and percolating inward from their borders. (b) By 2 months after the administration of NaIO$_3$ (shown in a different eye), the curvilinear patterns remained obvious but were much less distinct and more granular in appearance. (c) Corresponding DNIRA image shows a clear view to the underlying choroid devoid of an intact RPE monolayer in the region of hyperfluorescent FAF signal. To determine potential similarity to disease, four retina specialists were presented with standard images exemplifying or defining the patterns of hyperfluorescent FAF adjacent to GA coupled in 18 pairings; all four of them determined that the NaIO$_3$ images most closely resembled the diffuse trickling form of junctional hyperfluorescence. To demonstrate this, we show two reference images of the diffuse trickling pattern, insets (a) and (b), which are reproduced from Fleckenstein et al., *Invest Ophthalmol Vis Sci*, 55(5):2911–2920, 2014, and Fleckenstein et al., *Invest Ophthalmol Vis Sci*, 52:3761–3766, 2011, with the permission of ARVO.[8,20] (d) We also suggest marked similarity to LORD; figure reproduced with permission from Soumplis et al., *Acta Ophthalmol*, 91(3):191–195, 2013, with the permission of Blackwell Publishing.[75]

tative example (Fig. 4c), as the FAF pattern evolved and began to fill the area of RPE loss, significant deformation of the outer retina could be observed, accompanied by the accumulation of subretinal signal, some of which appeared as base-down triangles or spikes of hyperreflective signal (Fig. 4d), occasionally with a hollow center (Fig. 4e, asterisk). Further, thin projection images (slabs) derived from serial OCT images through the outer retina (Figs. 4e–4h) illustrate that the distinct 2D curvilinear or ovoid structures viewed en face correlate with the three-dimensional (3D) arrangement of these subretinal deposits. In a representative example of an en face slab (Fig. 4h), careful evaluation shows both a large and smaller adjacent circular structure corresponding to the accumulation of subretinal signal seen in cross-section.

Next, comparing FAF across even later timepoints, representative images show that, after the FAF pattern filled the entire region of damage, it matured in situ, becoming increasingly less distinct and more granular (Fig. 5). By 2 months (Fig. 5b), composite images show a marked reduction in intensity of the hyperfluorescent FAF pattern, that appears to subside or "burn out." Of note, and consistent with observations across all eyes from timepoints after day 3 post-NaIO$_3$ injection, DNIRA provided a clear view or "window defect" to the large underlying choroidal blood vessels, suggesting persistent disruption of an intact RPE monolayer (Fig. 5c).

With the overarching translational goal of identifying potential similarities between the hyperfluorescent patterns of FAF described in this study and those described in patients with GA, we then sought input from four retina specialists familiar with dry AMD. The senior author (SB) and three others (FA, LG, LU) evaluated 18 pairs of images comparing our rodent
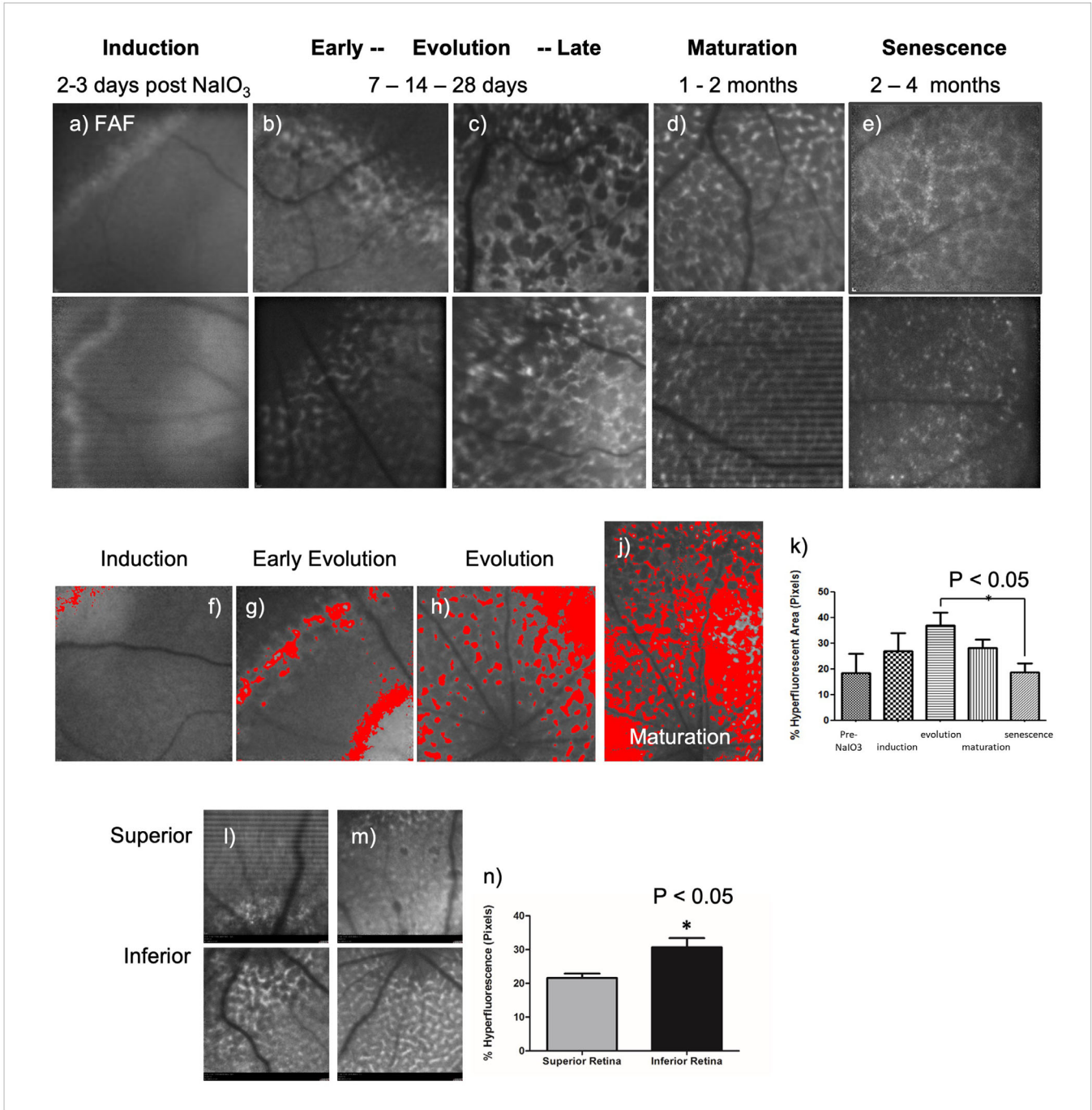
Figure 6. Proposed staging and quantifcation of changes in hyperfluorescent FAF patterns over time. (a–e) Two representative blue FAF images, extending from day 2 or 3 to 3 months after NaIO₃, are shown to illustrate the reproducible sequence of change that we describe as five stages: induction, evolution (early, middle, and late), maturation, and senescence. The approximate corresponding time period over which each stage appears is provided. A description of these changes in provided in Table. (f–j) Individual FAF images are readily analyzed quantitatively to determine the percentage of an image with supra-threshold fluorescence (illustrated in *red*). (j) Composite images can be more difficult to assess, as some areas are fully saturated. (k) Student's *t*-test confrmed a trend in overall autofluorescence between baseline and evolution, which signifcantly declined thereafter (*P* < 0.05). (l) Analysis of FAF images acquired at a single timepoint showed that small areas of damage appeared in the inferior retina before the upper, and threshold analysis within large areas of damage showed that (m) the pattern evolved more rapidly in the inferior than in the superior retina (n), confrmed by the increased level of autofluorescence (*P* < 0.05).

Table.   Stages of Atrophy Evolution

Induction	Early Evolution	Late Evolution	Maturation	Senescence
Isofluorescent blue FAF is observed within the region of NaIO$_3$-induced damage, with subtly hyperfluorescent borders. In small areas of RPE loss, the borders encircle the region, whereas in large areas they are located proximally surrounding the ONH and distally in the retinal periphery.	Widening borders assume complex curvilinear patterns of hyperfluorescent and isofluorescent FAF. Corresponding DNIRA and histology confirm the absence of the RPE layer.	Complex patterns that first formed at the borders percolate inward into the central region of RPE loss. In small regions, the borders may account for most of the pattern, obliterating the central region. In large areas of damage, the evolving patterns require weeks to involve the entire region of RPE loss. The inferior retina evolves more rapidly than the inferior.	Continued evolution of the FAF pattern eventually fills the region within the borders and matures in situ. At this point, the pattern is clearly evident.	After maturity is reached, the complex 2D pattern becomes far less obvious and finely granular, consistent with it "burning out."

results to standard images describing and defining clinical patterns of FAF.[7,9,53,74] Four out of the four retina specialists (100%) twice selected the diffuse trickling pattern as bearing the most similarity to our rodent images. Strikingly, none of the other patterns was selected even once. The most similar features included the highly curvilinear, looping, and arching hyperfluorescent patterns surrounding the ovoid regions of isofluorescence and the finely granular patterns that were especially evident in the late NaIO$_3$ time course (see inserts in Figs. 5a and 5b).[7,9,20,53] Outside of AMD, our lab noted marked similarity between the clearly defined curvilinear patterns in early FAF images, days 7 and 14, and observations reported in patients with late onset retinal degeneration (LORD) (Fig. 5d),[75] a rare monogenic degenerative disease that afflicts younger patients than does AMD.[75–78] Further, OCT images from patients with LORD can demonstrate hollow, base-down triangles (Fig. 5d, asterisk) with marked similarity to those we observed in the NaIO$_3$ model (Fig. 4g, asterisk).

Finally, in an effort to provide a useful tool to describe the changes in this model, and in keeping with the clinical practice of developing classification systems to describe complex ocular phenotypes, we propose a five-stage system consisting of induction, early evolution, late evolution (together forming a spectrum of evolution), maturation, and senescence. Two representative FAF images from each stage are shown in Figs. 6a to 6e), and a qualitative description of each is provided in the Table. As indicated, in addition to the spatiotemporal description of the hyperfluorescent FAF pattern, this classification system incorporates our observations that small patches are limited to the inferior fundus and mature quickly, rapidly filling their central gap, whereas in larger patches (360°) the pattern matures more rapidly inferiorly than superiorly. As such, phenotypes are described by their overall pattern, comparing border to central areas, and staged according to the most mature finding (whether small or large), thereby accommodating and incorporating the inter- and intra-animal variability not possible using a simple time course as descriptor.

Finally, in an effort to quantify the hyperfluorescent patterns, not just the size of the patch of damage, the area of bright image relative to the entire image was measured using a thresholding function (Image J) and compared against the baseline (pre-NaIO$_3$) image intensity. These data show that maximum brightness occurred during the evolution stage ($P < 0.05$) (Figs. 6f–6k) and declined thereafter. This method also confirmed the asymmetry between inferior and superior fundus ($P < 0.05$) (Figs. 6m–6o).

Discussion

Using clinically relevant cSLO imaging, this translational study uniquely described complex and evolving patterns of iso- and hyperfluorescent FAF in the days, weeks, and months following acute NaIO$_3$ challenge in the SD rat and provided multiple observations relevant first, to the model, second, to late non-exudative AMD, and third, to the use of this experimental paradigm for potential drug testing. We address each of these below.

First, although the NaIO$_3$ model has been described for 70 years,[65] by using composite blue FAF imaging throughout the entire fundus we can report that histologically confirmed, expansive regions of NaIO$_3$-induced PhR/RPE loss (1) were not hypofluorescent with the use of FAF; (2) were hypofluorescent with the use of DNIRA; (3) displayed reproducibly evolving, complex 2D patterns of iso- and hyperfluorescent FAF within their boundaries but not beyond; and (4) did not expand over time.

We suggest that the lack of profound hypofluorescent FAF within the histologically confirmed regions of RPE loss resulted from low levels of lipofuscin in the young, normal albino rat, which in turn makes in vivo detection of expansive areas of RPE loss less evident. Accordingly, to address and overcome this limitation, we used DNIRA to enhance detection of the RPE following ICG dye administration, and we can confirm here that regions of RPE loss did indeed appear profoundly hypofluorescent and well delineated, without terminal experimentation. Since the first description of DNIRA in the rat,[50] the ability for ICG to label human RPE in vivo has also been confirmed in the clinical setting in conjunction with ICG angiography and adaptive optics,[63,64] showing that this highly active monolayer internalizes ICG dye within the first 1 to 2 minutes following its IV injection. In one case, a study leveraged this observation to subtract the RPE signal from subsequent choriocapillaris filling, thus facilitating detection of the latter.[63] The DNIRA method has also been translated to the clinical setting in 12 patients, where it was reported to be insufficiently robust to identify inflammatory cells such as macrophages.[79]

We also report that, in 82 of 82 eyes (100%), complex, hyperfluorescent patterns of FAF emerged and evolved within regions of RPE loss, the widely accepted source of autofluorescence. This contrarian result suggests that a source other than the RPE is responsible for the signal. Current speculation includes the accumulation of autofluorescent debris in the expanded and deformed subretinal space, production of autofluorescent material within a cell type other than RPE, and/or the ingestion of hyperfluorescent material in inflammatory cells, and this topic is the subject of ongoing investigation. By contrast, finding that regions of NaIO$_3$-induced damage do not expand over time, even after several months, is consistent with the lack of hyperfluorescent signal beyond the areas of atrophy and potentially reflects the single and acute nature of the NaIO$_3$ insult. In the absence of ongoing stress or underlying tissue disease, atrophy has no impetus to expand.

Second, in addition to providing insights into the NaIO$_3$ model, this study provides a new preclinical approach with which to address hyperfluorescent FAF patterns observed in the clinical setting. As described for nearly 20 years, distinct hyperfluorescent FAF patterns predict different rates of GA expansion, and, although this classification system is generally thought to distinguish different subtypes of AMD, Mones and Biarnes[18] questioned a potential time-dependent element. Our results clearly describe temporal changes of hyperfluorescent FAF that follow acute NaIO$_3$. However, and to our complete surprise, as the patterns evolved and matured, they demonstrated a striking similarity to the diffuse trickling pattern form of late non-exudative AMD, supported by 100% consensus among the four retina specialists. Further supporting this interpretation and confirmed by our OCT findings, several reports have demonstrated the co-existence of the diffuse trickling pattern of FAF and subretinal drusenoid deposits (SDDs), also known as reticular pseudodrusen (RPDs), in up to 100% of eyes.[20,80,81] Clinical descriptions of SDDs/RPDs include the presence of shallow mounds, base-down triangles, and spikes in the subretinal space that evolve over time and are an independent risk factor for GA expansion, progression to late AMD, and systemic cardiovascular disease.[81–89] SDDs/RPDs have also been reported in several non-AMD degenerative conditions, including LORD and early macular atrophy with pseudodrusen.[75,76,80,90] It is therefore compelling that, following NaIO$_3$, the 2D curvilinear fluorescent patterns seen using FAF could be generated from 3D reconstructions of serial OCT sections of subretinal signal across multiple regions of interest, albeit in a small number of eyes ($n = 4$), a marked weakness of this paper. Taken together, we suggest that the findings in this study bear phenotypic similarity to aggressive, retinal degenerative disorders, and weigh in favor of a structural contribution to the 2D pattern of hyperfluorescent FAF signal. It is also therefore conceivable that the NaIO$_3$ model best mimics atrophy in the context of diffuse trickling disease and SDDs/RPDs, rather than AMD with classic, sub-RPE drusen. The detection of base-down triangles, hollow triangles, and spikes in both this model and disease also supports its potential relevance. Of note, we do not suggest that NaIO$_3$ recapitulates the etiology of these diseases.

This study also provides data that may be relevant to the clinical onset and evolution of nascent GA—in particular, the concept of outer retinal atrophy. In contrast to decades of clinical practice that defined GA as either absent or present, the recently developed

CAM consensus definition of GA now describes progressive ORA and RPE loss as a series of reproducible and orchestrated tissue changes. In particular, high-resolution OCT shows the clinical progression from iORA to cRORA,[49] with RPE preserved until last. As such, ORA has the potential to become a new therapeutic target, allowing atrophy to be arrested before it is complete. However, the inward to outward progression of clinical atrophy is contrary to the sequence of loss observed in the $NaIO_3$ model, which progresses instead from initial RPE loss to secondary ORA. Nonetheless, we suggest that this first description of evolving FAF in the absence of RPE provides a unique opportunity to investigate the process of outer retinal atrophy and the contribution of ORA to the FAF signal.

Also potentially relevant to the susceptibility of the human macula to AMD and other disease, we report the differential vulnerability of the superior and inferior rat fundus to $NaIO_3$-induced oxidative stress. Such differential vulnerability was previously reported in spontaneous and genetic murine models and may be especially relevant to small animals with overhead predators.[91–93] An unfortunate spatial vulnerability has been reported in patients who inadvertently received systemic $NaIO_3$ for the treatment of pneumothorax and developed bilateral macular atrophy.[44]

Third, from the perspective of using the $NaIO_3$ model to investigate much-needed treatments for non-exudative AMD, this paper also provides an opportunity to utilize patch size (area) as an in vivo measure of atrophy, but not atrophy expansion, without the need for terminal tissue analysis. It also shows that composite or widefield imaging of the rat fundus is required to fully appreciate the extent of $NaIO_3$ induced damage, particularly to its peripheral borders. Further, despite the positive correlation between $NaIO_3$ dose and the area of atrophy, we have demonstrated that this in turn influences the relative proportion of expanding border to spared mid-region, with smaller areas paradoxically maturing more rapidly than larger ones. These findings could have significant implications for preclinical drug testing when selecting regions of tissue for OCT, histological, or biochemical analysis, without taking these spatiotemporal changes into account. This study also suggests that methodologically, the emergence and evolving tissue changes of ORA can be investigated preclinically and that DNIRA serves to enhance detection of the rodent RPE, and therefore regions of its loss,[50] making it a useful preclinical imaging method to detect atrophy due to any cause.

Taken together, we suggest this in vivo imaging study supports a general hypothesis that atrophy is an evolving tissue process, not just the absence of tissue, and that complex and changing hyperfluorescent that blue FAF patterns derived from the outer retina can occur in the absence of RPE. As such, careful evaluation of models of atrophy, like ocular models of neovascularization that led to today's anti-angiogenic therapies, have the potential to support the development of much-needed treatments for the blinding complications of late non-exudative AMD.

Acknowledgments

References

1. Liao DS, Grossi FV, El Mehdi D, et al. Complement C3 inhibitor pegcetacoplan for geographic atrophy secondary to age-related macular degeneration: a randomized phase 2 trial. *Ophthalmology*. 2020;127:186–195.
2. Jack LS, Sadiq MA, Do DV, Nguyen QD. Emixustat and lampalizumab: potential therapeutic options for geographic atrophy. *Dev Ophthalmol*. 2016;55:302–309.
3. Holz FG, Strauss EC, Schmitz-Valckenberg S, van Lookeren Campagne M. Geographic atrophy: clinical features and potential therapeutic approaches. *Ophthalmology*. 2014;121:1079–1091.
4. Yaspan BL, Williams DF, Holz FG, et al. Targeting factor D of the alternative complement pathway reduces geographic atrophy progression secondary to age-related macular degeneration. *Sci Transl Med*. 2017;9:eaaf1443.

5. Wolf-Schnurrbusch UE, Wittwer VV, Ghanem R, et al. Blue-light versus green-light autofluorescence: lesion size of areas of geographic atrophy. *Invest Ophthalmol Vis Sci*. 2011;52:9497–9502.

6. Holz FG, Sadda SR, Busbee B, et al. Efficacy and safety of lampalizumab for geographic atrophy due to age-related macular degeneration: Chroma and Spectri phase 3 randomized clinical trials. *JAMA Ophthalmol*. 2018;136:666–677.

7. Bindewald A, Schmitz-Valckenberg S, Jorzik JJ, et al. Classification of abnormal fundus autofluorescence patterns in the junctional zone of geographic atrophy in patients with age related macular degeneration. *Br J Ophthalmol*. 2005;89:874–878.

8. Fleckenstein M, Schmitz-Valckenberg S, Martens C, et al. Fundus autofluorescence and spectral-domain optical coherence tomography characteristics in a rapidly progressing form of geographic atrophy. *Invest Ophthalmol Vis Sci*. 2011;52:3761–3766.

9. Holz FG, Bindewald-Wittich A, Fleckenstein M, et al. Progression of geographic atrophy and impact of fundus autofluorescence patterns in age-related macular degeneration. *Am J Ophthalmol*. 2007;143:463–472.

10. Jeong YJ, Hong IH, Chung JK, Kim KL, Kim HK, Park SP. Predictors for the progression of geographic atrophy in patients with age-related macular degeneration: fundus autofluorescence study with modified fundus camera. *Eye (Lond)*. 2014;28:209–218.

11. Ly A, Nivison-Smith L, Assaad N, Kalloniatis M. Fundus autofluorescence in age-related macular degeneration. *Optom Vis Sci*. 2017;94:246–259.

12. Shen LL, Liu F, Nardini HG, Del Priore LV. Reclassification of fundus autofluorescence patterns surrounding geographic atrophy based on progression rate: a systematic review and meta-analysis. *Retina*. 2019;39:1829–1839.

13. Delori FC, Dorey CK, Staurenghi G, Arend O, Goger DG, Weiter JJ. In vivo fluorescence of the ocular fundus exhibits retinal pigment epithelium lipofuscin characteristics. *Invest Ophthalmol Vis Sci*. 1995;36:718–729.

14. Han M, Giese G, Schmitz-Valckenberg S, et al. Age-related structural abnormalities in the human retina-choroid complex revealed by two-photon excited autofluorescence imaging. *J Biomed Opt*. 2007;12:024012.

15. Holz FG, Bellman C, Staudt S, Schutt F, Volcker HE. Fundus autofluorescence and development of geographic atrophy in age-related macular degeneration. *Invest Ophthalmol Vis Sci*. 2001;42:1051–1056.

16. Holz FG, Bellmann C, Margaritidis M, Schutt F, Otto TP, Volcker HE. Patterns of increased in vivo fundus autofluorescence in the junctional zone of geographic atrophy of the retinal pigment epithelium associated with age-related macular degeneration. *Graefes Arch Clin Exp Ophthalmol*. 1999;237:145–152.

17. Biarnes M, Mones J, Trindade F, Alonso J, Arias L. Intra and interobserver agreement in the classification of fundus autofluorescence patterns in geographic atrophy secondary to age-related macular degeneration. *Graefes Arch Clin Exp Ophthalmol*. 2012;250:485–490.

18. Mones J, Biarnes M. Geographic atrophy phenotype identification by cluster analysis. *Br J Ophthalmol*. 2018;102:388–392.

19. Biarnes M, Forero CG, Arias L, Alonso J, Mones J. Reappraisal of geographic atrophy patterns seen on fundus autofluorescence using a latent class analysis approach. *Invest Ophthalmol Vis Sci*. 2014;55:8302–8308.

20. Fleckenstein M, Schmitz-Valckenberg S, Lindner M, et al. The "diffuse-trickling" fundus autofluorescence phenotype in geographic atrophy. *Invest Ophthalmol Vis Sci*. 2014;55:2911–2920.

21. Batioglu F, Gedik Oguz Y, Demirel S, Ozmert E. Geographic atrophy progression in eyes with age-related macular degeneration: role of fundus autofluorescence patterns, fellow eye and baseline atrophy area. *Ophthalmic Res*. 2014;52:53–59.

22. Lindner M, Bezatis A, Czauderna J, et al. Choroidal thickness in geographic atrophy secondary to age-related macular degeneration. *Invest Ophthalmol Vis Sci*. 2015;56:875–882.

23. Lin KH, Tran T, Kim S, et al. Age-related changes in the rhesus macaque eye. *Exp Eye Res*. 2021;212:108754.

24. Soundara Pandi SP, Ratnayaka JA, Lotery AJ, Teeling JL. Progress in developing rodent models of age-related macular degeneration (AMD). *Exp Eye Res*. 2021;203:108404.

25. Pennesi ME, Neuringer M, Courtney RJ. Animal models of age related macular degeneration. *Mol Aspects Med*. 2012;33:487–509.

26. Zeiss CJ. Animals as models of age-related macular degeneration: an imperfect measure of the truth. *Vet Pathol*. 2010;47:396–413.

27. Grossniklaus HE, Kang SJ, Berglin L. Animal models of choroidal and retinal neovascularization. *Prog Retin Eye Res*. 2010;29:500–519.

translational vision science & technology

28. Liu CH, Wang Z, Sun Y, Chen J. Animal models of ocular angiogenesis: from development to pathologies. *FASEB J*. 2017;31:4665–4681.

29. Montezuma SR, Vavvas D, Miller JW. Review of the ocular angiogenesis animal models. *Semin Ophthalmol*. 2009;24:52–61.

30. Ryan SJ. The development of an experimental model of subretinal neovascularization in disciform macular degeneration. *Trans Am Ophthalmol Soc*. 1979;77:707–745.

31. Frank RN. Argon laser photocoagulation and subretinal neovascularization. *Ophthalmic Surg*. 1974;5:56–64.

32. Dobi ET, Puliafito CA, Destro M. A new model of experimental choroidal neovascularization in the rat. *Arch Ophthalmol*. 1989;107:264–269.

33. Frank RN, Das A, Weber ML. A model of subretinal neovascularization in the pigmented rat. *Curr Eye Res*. 1989;8:239–247.

34. Pierce EA, Foley ED, Smith LE. Regulation of vascular endothelial growth factor by oxygen in a model of retinopathy of prematurity. *Arch Ophthalmol*. 1996;114:1219–1228.

35. Smith LE, Wesolowski E, McLellan A, et al. Oxygen-induced retinopathy in the mouse. *Invest Ophthalmol Vis Sci*. 1994;35:101–111.

36. Ozaki H, Seo MS, Ozaki K, et al. Blockade of vascular endothelial cell growth factor receptor signaling is sufficient to completely prevent retinal neovascularization. *Am J Pathol*. 2000;156:697–707.

37. Tobe T, Okamoto N, Vinores MA, et al. Evolution of neovascularization in mice with overexpression of vascular endothelial growth factor in photoreceptors. *Invest Ophthalmol Vis Sci*. 1998;39:180–188.

38. Hanus J, Anderson C, Wang S. RPE necroptosis in response to oxidative stress and in AMD. *Ageing Res Rev*. 2015;24:286–298.

39. Tong Y, Wang S. Not all stressors are equal: mechanism of stressors on RPE cell degeneration. *Front Cell Dev Biol*. 2020;8:591067.

40. Sorsby A, Harding R. Oxidizing agents as potentiators of the retinotoxic action of sodium fluoride, sodium iodate and sodium iodoacetate. *Nature*. 1966;210:997–998.

41. Korte GE, Gerszberg T, Pua F, Henkind P. Choriocapillaris atrophy after experimental destruction of the retinal pigment epithelium in the rat. A study in thin sections and vascular casts. *Acta Anat (Basel)*. 1986;127:171–175.

42. Chowers G, Cohen M, Marks-Ohana D, et al. Course of sodium iodate-induced retinal degeneration in albino and pigmented mice. *Invest Ophthalmol Vis Sci*. 2017;58:2239–2249.

43. Enzmann V, Row BW, Yamauchi Y, et al. Behavioral and anatomical abnormalities in a sodium iodate-induced model of retinal pigment epithelium degeneration. *Exp Eye Res*. 2006;82:441–448.

44. Wagenfeld L, Zeitz O, Richard G. Visual loss after povidone-iodine pleurodesis. *N Engl J Med*. 2007;357:1264–1265.

45. Zhao J, Kim HJ, Sparrow JR. Multimodal fundus imaging of sodium iodate-treated mice informs RPE susceptibility and origins of increased fundus autofluorescence. *Invest Ophthalmol Vis Sci*. 2017;58:2152–2159.

46. Ou Q, Zhu T, Li P, et al. Establishment of retinal degeneration model in rat and monkey by intravitreal injection of sodium iodate. *Curr Mol Med*. 2018;18:352–364.

47. Bhutto IA, Ogura S, Baldeosingh R, McLeod DS, Lutty GA, Edwards MM. An acute injury model for the phenotypic characteristics of geographic atrophy. *Invest Ophthalmol Vis Sci*. 2018;59:AMD143–AMD151.

48. Guymer RH, Rosenfeld PJ, Curcio CA, et al. Incomplete retinal pigment epithelial and outer retinal atrophy in age-related macular degeneration: Classification of Atrophy Meeting report 4. *Ophthalmology*. 2020;127:394–409.

49. Sadda SR, Guymer R, Holz FG, et al. Consensus definition for atrophy associated with age-related macular degeneration on OCT: Classification of Atrophy report 3. *Ophthalmology*. 2018;125:537–548.

50. Pankova N, Zhao X, Liang H, Baek DS, Wang H, Boyd S. Delayed near-infrared analysis permits visualization of rodent retinal pigment epithelium layer in vivo. *J Biomed Opt*. 2014;19:076007.

51. Biswal MR, Ildefonso CJ, Mao H, et al. Conditional induction of oxidative stress in RPE: a mouse model of progressive retinal degeneration. *Adv Exp Med Biol*. 2016;854:31–37.

52. Boretsky A, Motamedi M, Bell B, van Kuijk F. Quantitative evaluation of retinal response to laser photocoagulation using dual-wavelength fundus autofluorescence imaging in a small animal model. *Invest Ophthalmol Vis Sci*. 2011;52:6300–6307.

53. Fritsche LG, Fleckenstein M, Fiebig BS, et al. A subgroup of age-related macular degeneration is associated with mono-allelic sequence variants in the ABCA4 gene. *Invest Ophthalmol Vis Sci*. 2012;53:2112–2118.

54. Pfaffl MW, Horgan GW, Dempfle L. Relative expression software tool (REST) for group-wise comparison and statistical analysis of relative

expression results in real-time PCR. *Nucleic Acids Res*. 2002;30:e36.

55. Joshi R, Pankova N, Wang H, et al. Spontaneously occurring fundus findings observed using confocal scanning laser ophthalmoscopy in wild type Sprague Dawley rats. *Regul Toxicol Pharmacol* 2016;77:160–166.

56. Delori FC, Goger DG, Dorey CK. Age-related accumulation and spatial distribution of lipofuscin in RPE of normal subjects. *Invest Ophthalmol Vis Sci*. 2001;42:1855–1866.

57. Lois N, Halfyard AS, Bunce C, Bird AC, Fitzke FW. Reproducibility of fundus autofluorescence measurements obtained using a confocal scanning laser ophthalmoscope. *Br J Ophthalmol*. 1999;83:276–279.

58. von Ruckmann A, Fitzke FW, Bird AC. Distribution of fundus autofluorescence with a scanning laser ophthalmoscope. *Br J Ophthalmol*. 1995;79:407–412.

59. von Ruckmann A, Fitzke FW, Bird AC. Fundus autofluorescence in age-related macular disease imaged with a laser scanning ophthalmoscope. *Invest Ophthalmol Vis Sci*. 1997;38:478–486.

60. von Ruckmann A, Fitzke FW, Bird AC. Distribution of pigment epithelium autofluorescence in retinal disease state recorded in vivo and its change over time. *Graefes Arch Clin Exp Ophthalmol*. 1999;237:1–9.

61. Sparrow JR, Gregory-Roberts E, Yamamoto K, et al. The bisretinoids of retinal pigment epithelium. *Prog Retin Eye Res*. 2012;31:121–135.

62. Sparrow JR, Yoon KD, Wu Y, Yamamoto K. Interpretations of fundus autofluorescence from studies of the bisretinoids of the retina. *Invest Ophthalmol Vis Sci*. 2010;51:4351–4357.

63. Jung H, Liu T, Liu J, Huryn LA, Tam J. Combining multimodal adaptive optics imaging and angiography improves visualization of human eyes with cellular-level resolution. *Commun Biol*. 2018;1:189.

64. Tam J, Liu J, Dubra A, Fariss R. In vivo imaging of the human retinal pigment epithelial mosaic using adaptive optics enhanced indocyanine green ophthalmoscopy. *Invest Ophthalmol Vis Sci*. 2016;57:4376–4384.

65. Sorsby A. Experimental pigmentary degeneration of the retina by sodium iodate. *Br J Ophthalmol*. 1941;25:58–62.

66. Kiuchi K, Yoshizawa K, Shikata N, Moriguchi K, Tsubura A. Morphologic characteristics of retinal degeneration induced by sodium iodate in mice. *Curr Eye Res*. 2002;25:373–379.

67. Machalińska A, Lubiński W, Kłos P, et al. Sodium iodate selectively injuries the posterior pole of the retina in a dose-dependent manner: morphological and electrophysiological study. *Neurochem Res*. 2010;35:1819–1827.

68. Kannan R, Hinton DR. Sodium iodate induced retinal degeneration: new insights from an old model. *Neural Regen Res*. 2014;9:2044–2045.

69. Machalinska A, Lejkowska R, Duchnik M, et al. Dose-dependent retinal changes following sodium iodate administration: application of spectral-domain optical coherence tomography for monitoring of retinal injury and endogenous regeneration. *Curr Eye Res*. 2014;39:1033–1041.

70. Moriguchi M, Nakamura S, Inoue Y, et al. Irreversible photoreceptors and RPE cells damage by intravenous sodium iodate in mice is related to macrophage accumulation. *Invest Ophthalmol Vis Sci*. 2018;59:3476–3487.

71. Liu Y, Li Y, Wang C, Zhang Y, Su G. Morphologic and histopathologic change of sodium iodate-induced retinal degeneration in adult rats. *Int J Clin Exp Pathol*. 2019;12:443–454.

72. Baek DS, Liang H, Zhao X, Pankova N, Wang H, Boyd S. Fundus autofluorescence (FAF) non-invasively identifies chorioretinal toxicity in a rat model of retinal pigment epithelium (RPE) damage. *J Pharmacol Toxicol Methods*. 2015;71:77–82.

73. Hariri S, Tam MC, Lee D, Hileeto D, Moayed AA, Bizheva K. Noninvasive imaging of the early effect of sodium iodate toxicity in a rat model of outer retina degeneration with spectral domain optical coherence tomography. *J Biomed Opt*. 2013;18:26017.

74. Mones J, Biarnes M. The rate of progression of geographic atrophy decreases with increasing baseline lesion size even after the square root transformation. *Transl Vis Sci Technol*. 2018;7:40.

75. Soumplis V, Sergouniotis PI, Robson AG, et al. Phenotypic findings in C1QTNF5 retinopathy (late-onset retinal degeneration). *Acta Ophthalmol*. 2013;91:e191–195.

76. Vincent A, Munier FL, Vandenhoven CC, Wright T, Westall CA, Heon E. The characterization of retinal phenotype in a family with C1QTNF5-related late-onset retinal degeneration. *Retina*. 2012;32:1643–1651.

77. Chekuri A, Zientara-Rytter K, Soto-Hermida A, et al. Late-onset retinal degeneration pathology due to mutations in CTRP5 is mediated through HTRA1. *Aging Cell*. 2019;18:e13011.

78. Stanton CM, Borooah S, Drake C, et al. Novel pathogenic mutations in C1QTNF5 support a

dominant negative disease mechanism in late-onset retinal degeneration. *Sci Rep*. 2017;7:12147.

79. Bell OH, Carreno E, Williams EL, et al. Intravenous indocyanine green dye is insufficient for robust immune cell labelling in the human retina. *PLoS One*. 2020;15:e0226311.

80. Fleckenstein M, Grassmann F, Lindner M, et al. Distinct genetic risk profile of the rapidly progressing diffuse-trickling subtype of geographic atrophy in age-related macular degeneration (AMD). *Invest Ophthalmol Vis Sci*. 2016;57:2463–2471.

81. Querques G, Blanco R, Puche N, Massamba N, Souied EH. Extensive macular atrophy with pseudodrusen-like appearance. *Ophthalmology*. 2013;120:429.e1–2.

82. Zhang Y, Wang X, Sadda SR, et al. Lifecycles of individual subretinal drusenoid deposits and evolution of outer retinal atrophy in age-related macular degeneration. *Ophthalmol Retina*. 2020;4:274–283.

83. Zweifel SA, Spaide RF, Curcio CA, Malek G, Imamura Y. Reticular pseudodrusen are subretinal drusenoid deposits. *Ophthalmology*. 2010;117:303–312.e1.

84. Nassisi M, Lei J, Abdelfattah NS, et al. OCT risk factors for development of late age-related macular degeneration in the fellow eyes of patients enrolled in the HARBOR study. *Ophthalmology*. 2019;126:1667–1674.

85. Maguire MG, Fine SL. Reticular pseudodrusen. *Retina*. 1996;16:167–168.

86. Arnold JJ, Sarks SH, Killingsworth MC, Sarks JP. Reticular pseudodrusen. A risk factor in age-related maculopathy. *Retina*. 1995;15:183–191.

87. Zweifel SA, Imamura Y, Spaide TC, Fujiwara T, Spaide RF. Prevalence and significance of subretinal drusenoid deposits (reticular pseudodrusen) in age-related macular degeneration. *Ophthalmology*. 2010;117:1775–1781.

88. Querques G, Canoui-Poitrine F, Coscas F, et al. Analysis of progression of reticular pseudodrusen by spectral domain-optical coherence tomography. *Invest Ophthalmol Vis Sci*. 2012;53:1264–1270.

89. Spaide RF. Outer retinal atrophy after regression of subretinal drusenoid deposits as a newly recognized form of late age-related macular degeneration. *Retina*. 2013;33:1800–1808.

90. Spaide RF. Age-related choroidal atrophy. *Am J Ophthalmol*. 2009;147:801–810.

91. Sakami S, Maeda T, Bereta G, et al. Probing mechanisms of photoreceptor degeneration in a new mouse model of the common form of autosomal dominant retinitis pigmentosa due to P23H opsin mutations. *J Biol Chem*. 2011;286:10551–10567.

92. Smit-McBride Z, Oltjen SL, Lavail MM, Hjelmeland LM. A strong genetic determinant of hyperoxia-related retinal degeneration on mouse chromosome 6. *Invest Ophthalmol Vis Sci*. 2007;48:405–411.

93. Ollivier FJ, Samuelson DA, Brooks DE, Lewis PA, Kallberg ME, Komaromy AM. Comparative morphology of the tapetum lucidum (among selected species). *Vet Ophthalmol*. 2004;7:11–22.

94. Fritsche LG, Igl W, Bailey JN, et al. A large genome-wide association study of age-related macular degeneration highlights contributions of rare and common variants. *Nat Genet*. 2016;48:134–143.